

Thermal Infrared Near-Field Spectroscopy

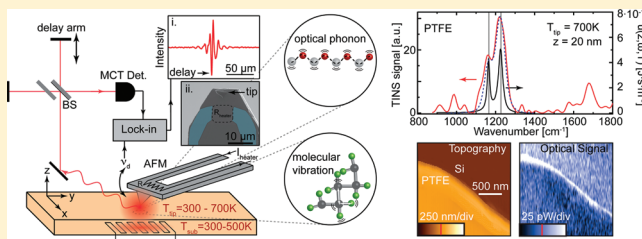
Andrew C. Jones and Markus B. Raschke*

Department of Physics, Department of Chemistry, and JILA, University of Colorado, Boulder, Colorado 80309, United States

S Supporting Information

ABSTRACT: Despite the seminal contributions of Kirchhoff and Planck describing far-field thermal emission, fundamentally distinct spectral characteristics of the electromagnetic thermal near-field have been predicted. However, due to their evanescent nature their direct experimental characterization has remained elusive. Combining scattering scanning near-field optical microscopy with Fourier-transform spectroscopy using a heated atomic force microscope tip as both a local thermal source and scattering probe, we spectroscopically characterize the thermal near-field in the mid-infrared. We observe the spectrally distinct and orders of magnitude enhanced resonant spectral near-field energy density associated with vibrational, phonon, and phonon–polariton modes. We describe this behavior and the associated distinct on- and off-resonance nanoscale field localization with model calculations of the near-field electromagnetic local density of states. Our results provide a basis for intrinsic and extrinsic resonant manipulation of optical forces, control of nanoscale radiative heat transfer with optical antennas, and use of this new technique of thermal infrared near-field spectroscopy for broadband chemical nanospectroscopy.

KEYWORDS: Thermal near-fields, vibrational spectroscopy, near-field imaging, chemical spectroscopy, evanescent fields



For over a century the laws of Kirchhoff¹ and Planck² have fully described far-field thermal emission, the fundamental origin of which lies in the microscopic space-time fluctuation of charge carriers. However, studies of the electromagnetic thermal near-field have recently emphasized fundamentally distinct spectral, spatial, and coherence properties at sub-wavelength dimensions for solid media.^{3–7} The properties of thermal near-fields determine important near-surface phenomena including not only nanoscale radiative heat transfer^{8,9} but also the van der Waals/Casimir-Polder forces originating in the zero-point fluctuations or induced by the thermal fluctuations as first shown by Lifshitz and demonstrated by off-resonance interaction at a dielectric surface.^{10–13} One of the most fascinating results of recent theoretical predictions^{5–7,14} is the resonant enhancement of the near-field spectral energy density when associated with either intrinsic electronic and vibrational excitations or extrinsic geometric resonances of the medium. Despite its influence on and possibility for control of the above phenomena via resonant interaction, experimental investigations of the spectral distribution of the electromagnetic thermal near-field have remained difficult due to its purely evanescent character.^{15–18}

The transition of the underlying spectral energy density $u[z, \omega, T]$ from the far- to near-field regime can be described as the product of the electromagnetic local density of states (EM-LDOS) $\rho[z, \omega]$ with the Planck distribution for the mean energy of an oscillator $\Theta[\omega, T] = \hbar\omega / (\exp[\hbar\omega/k_B T] - 1)$ [ref 6] as $u[z, \omega, T] = \Theta[\omega, T] \cdot \rho[z, \omega]$. For the determination of the EM-LDOS, the relationship of a fluctuating current density element within a medium of dielectric permittivity ϵ_2 to its resulting field induced above the surface is established via the

dyadic Green function for the system geometry.⁶ Through application of the fluctuation–dissipation theorem,^{6,19} which incorporates the statistical properties of the current density distribution, the EM-LDOS can be expressed as a sum of far-field radiative and near-field evanescent solutions (see Appendix for further details).

The evanescent component of the EM-LDOS is drastically enhanced in the presence of vibrational or electronic surface resonances. While far-field thermal radiation is most often characterized by broadband blackbody-like emission, systems with characteristic surface resonances have been predicted to exhibit a near-monochromatic (vibrational lifetime limited) spectral energy density distribution in the near-field limit.⁵ In this quasistatic near-field regime for $z \ll \lambda$, the evanescent EM-LDOS can be approximated as^{6,7}

$$\rho_{\text{evan}}[z, \omega] \simeq \frac{1}{4\pi^2 \omega z^3} \frac{\text{Im}[\epsilon_2]}{|\epsilon_2 + 1|^2} \quad (1)$$

This relation illustrates the resulting strong enhancement of the EM-LDOS on resonance either in $\text{Im}[\epsilon_2]$ or via the surface polariton resonance condition $\text{Re}[\epsilon_2] = -1$.

In this work, we demonstrate the generation, evanescent field scattering, and interferometric detection of thermal near-fields using scattering scanning near-field optical microscopy (*s*-SNOM) in a novel implementation with heated thermal atomic force microscope tips. With this technique of thermal infrared

Received: November 29, 2011

Revised: January 10, 2012

Published: January 26, 2012

near-field spectroscopy (TINS), we identify the enhanced and spectrally narrow evanescent fields associated with different molecular vibrational and surface phonon polariton modes. The observed spectral characteristics are fundamentally distinct from corresponding far-field emission and reflect the underlying near-field distribution of the spectral energy density and the associated resonantly enhanced EM-LDOS.

The experimental layout is shown in Figure 1. The setup is based on an atomic force microscope (AFM, CP-Research,

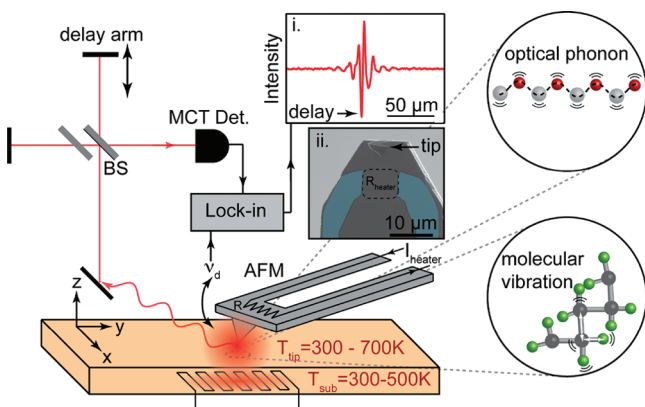


Figure 1. Experimental setup for thermal infrared near-field spectroscopy measurements with thermal near-field radiation scattered by the tip and spectrally resolved via a Michelson-type FTIR interferometer (inset i: typical interferogram). Both the surface or a specialized AFM tip (inset ii) can be heated resistively with the tip in dynamic force feedback. The evanescent thermal near-field exhibits resonant enhancement via molecular or phonon resonances.

Veeco Inc.) operating in noncontact dynamic force mode and has been modified to allow for independent control of sample and tip temperature. The thermal evanescent fields induced via sample or tip heating^{16,17} are scattered by the AFM tip into detectable far-field radiation. This tip-scattered thermal radiation is collected using a Cassegrain-type reflective objective (NA = 0.5, not shown) oriented at an angle of 60° with respect to the surface normal, directed through a Michelson interferometer, and detected by a mercury-cadmium-telluride (MCT) detector (Kolmar, Model KLD-0.25/DC/11.5) from 5.5–12 μm; the detector spectral range is limited by the detector bandgap at the long-wavelengths and the achievable temperature/detector sensitivity at shorter wavelengths. Discrimination of the near-field signal against the far-field emission/scattering is performed by lock-in filtering on the fundamental frequency of the AFM tip-dither frequency ν_d .^{20,21}

A resistive sample heater controls the sample temperature in the 300–500 K range with upper limit set by stable AFM scanning conditions. Specially designed AFM probes (Anasys Instruments, AN2-200) allow for resistive tip heating up to ~700 K (Figure 1, inset ii). These probes have been further modified by focused-ion beam milling for free line of sight optical access to the tip-sample apex region.

The advantage of the use of heated AFM probes is that they allow for stable scanning conditions to be maintained with higher temperatures in the tip-sample gap region compared to either sample heating or active heating of both tip and sample. With the heated AFM tip in close proximity to the material surface, efficient localized heat transfer occurs via ballistic thermal air conduction.²² Using localized surface melting of

polycarbonate samples allowed us to gauge the surface temperatures near the tip to be at least ~550 K with the AFM operating in noncontact force feedback mode. Note that for the purpose of our study discussed here, exact knowledge of the surface temperature is not critical. Surface temperature primarily affects the signal intensity and, only to a minor extent, the spectral characteristics of the near-field energy density distribution.

The spectral distribution of the scattered thermal light from the heated tip-sample gap region is reconstructed via interferometric FTIR detection. With the use of a dielectric tip material (Si) that is off-resonant and thus spectrally broadband in the infrared spectral range of interest (5.5–12 μm), the tip-scattered light reflects the intrinsic vibrational/phonon resonances of the sample surface.^{6,23} We choose polytetrafluoroethylene (PTFE) with its characteristic C–F stretch modes, as a representative molecular solid, and use natural SiO₂ quartz and SiC as crystalline solids with collective phonon and phonon-polariton excitations.

Figure 2 (a–c, red lines, upper panels) shows the tip-scattered thermal near-field signal for SiC, SiO₂, and PTFE, respectively, using a heated tip at ~700 K. For all three materials peaked near-field spectral signal distributions are observed associated with the respective molecular or surface phonon polariton (SPhP) resonances as discussed below. For comparison, the expected spectral energy density distribution $u[z, \omega, T]$ at 20 nm above the surface is calculated for the three materials using literature values for the respective complex dielectric function (a–c, black lines, upper panels)^{24,25} following the exact procedure discussed in the Appendix (i.e., beyond the quasistatic approximation). The corresponding relative far-field thermal emission spectra from the three heated materials measured with the AFM tip retracted are shown (a–c, red lines, lower panels) normalized against emission from a Si surface. They exhibit a signal decrease near the respective resonances in accordance with Kirchhoff's law of thermal emission for opaque bodies (Figure 2a–c, black line, lower panels).²⁶

As can be seen for SiC, a peaked near-field signal occurs near ~945 cm⁻¹; for SiO₂ it is observed between 1150 and 1205 cm⁻¹. These spectral peaks correspond to the SPhP resonance modes of the respective materials. The SPhP resonance condition is met in SiC at ~950 cm⁻¹ while for SiO₂ it is met both at ~1157 and 1190 cm⁻¹. As a nondispersive molecular solid PTFE does not meet the conditions for surface wave excitation. Its distinct molecular resonances located at 1158, 1210, and 1240 cm⁻¹ (latter two spectrally not resolved) are associated with the different C–F symmetric ω_S and antisymmetric ω_{AS} vibrational stretch modes.^{27,28} The measured signal magnitude is slightly weaker compared to that from polaritonic materials.

The observed resonant near-field characteristics are fundamentally distinct from the manifestation of these resonances in far-field emission, scattering, and reflection. SiC exhibits a reduction in far-field emissivity below ~1000 cm⁻¹ which marks the onset of the high reflectivity Reststrahlen band (800–1000 cm⁻¹). The measured emission from SiO₂ shows slight dips corresponding to enhanced reflectivity associated with the series of LO and TO Si–O phonon modes (1050–1250 cm⁻¹).^{29,30} The PTFE film further exhibits reduced emissivity in the vicinity of the C–F vibrational modes, albeit weaker, due to the lower vibrational density of states compared to that of the optical phonon modes in SiC or SiO₂.

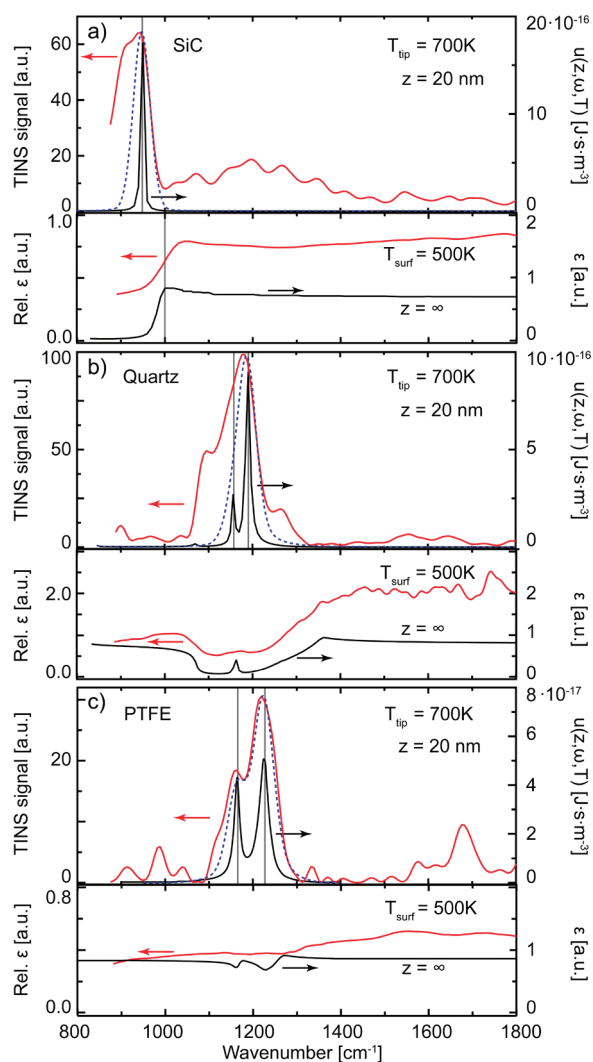


Figure 2. Tip-scattered enhanced thermal near-field signal (upper panels, red lines, a–c) for SiC, SiO₂, and PTFE, associated with the characteristic phonon-polariton, phonon, and vibrational resonances. The spectral energy density associated with the EM-LDOS (upper panels, black lines, a–c), calculated for $z = 20$ nm and $T = 500$ K, is concurrently displayed in the figure with the simulated spectral distribution of the TINS signal (blue dashed lines, a–c, arbitrary units). In contrast, far-field thermal emission from heated substrates (lower panels, red lines, a–c) exhibit signal decreases associated with elevated reflectivity on resonance in agreement with calculated far-field thermal emissivity given by Kirchhoff's law (lower panels, black lines, a–c).

In order to verify the near-field origin of the observed behavior, we measured a series of near-field spectra as a function of distance above the sample surface and observed peaked TINS signals associated with the expected resonances of the EM-LDOS up to a height of ~ 1 μm above the sample surface. As an example the corresponding tip–sample distance dependence of the integrated combined ω_S and ω_{AS} modes for PTFE (1100 – 1300 cm^{-1}) is shown in Figure 3 (red solid circles) (see Supporting Information for corresponding measurements on SiC). A strong near-field confinement below ~ 200 nm is found. The corresponding parameter free on-resonance model calculation of the distance dependence of the expected TINS signal derived from the spectral energy density above PTFE is shown as the solid line.³¹

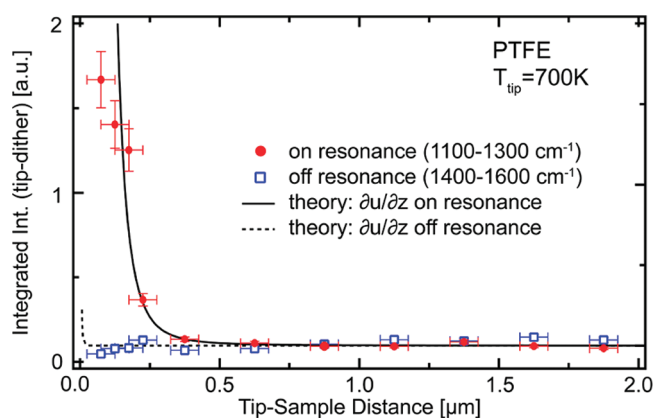


Figure 3. Distance dependence for the integrated spectral intensity on- (1100 – 1300 cm^{-1}) and off-resonance (1400 – 1600 cm^{-1}) for PTFE in comparison to corresponding model calculations (solid and dashed lines) exhibiting strong near-field localization.

In contrast, the off-resonant signal contribution (here integrated from 1400 – 1600 cm^{-1}) does not exhibit a discernible increase (blue open squares) within the uncertainty of the experiment. This behavior is also reproduced by the corresponding off-resonant calculation (dashed line) which only exhibits a weak increase at very short distances (< 50 nm).^{6,7}

The origin and consequences of the difference between the far- and near-field spectral behavior, its distance dependence, and its material specific resonant and nonresonant relationship with molecular vibrations, optical phonons, or surface polariton modes can be understood from an in-plane wavevector k_{\parallel} dependent analysis of the spectral distribution of the EM-LDOS calculated using eq 4 (Appendix) and displayed in Figure 4. In the far-field regime ($z \gg \lambda$, $k_{\parallel} < k_0$), materials generally act as broadband emitters with decreased emissivity associated with increased reflectivity. This corresponds to $k_{\parallel} < k_0$ for far-field emission with k_0 representing the free space wavevector (white dashed line). In the transition from the far- to the near-field (i, ii, iii), the contributions to the total EM-LDOS from states with large in-plane wavevector components k_{\parallel} begins to become significant. Due to the large on-resonance contributions from the evanescent modes to the EM-LDOS, which increase with decreasing distance much faster than the off-resonance contributions, the initial onset of the near-field regime occurs at larger distances at resonant frequencies (as seen in the data in Figure 3).

Under conditions for surface wave excitation ($\text{Re}[\epsilon_2] < -1$), enhancement of the EM-LDOS associated with evanescent fields begins near $z \simeq \lambda$. Here, states with k_{\parallel} satisfying the polariton dispersion relation $k_{\parallel} = (\omega/c)[\epsilon_2/(\epsilon_2 + 1)]^{1/2}$ start to become the principal contribution to the EM-LDOS. In close proximity to the surface ($z \ll \lambda$), the EM-LDOS lies in the quasi-static regime where it is dominated by large in-plane wavevector states ($k_{\parallel} \gg k_0$) at frequencies where $\text{Im}[\epsilon_2]$ is maximal or the surface polariton resonance condition $\text{Re}[\epsilon_2] = -1$ is met as can be seen from eq 1 (please see Appendix for further details).

This behavior is shown specifically for materials without (Figure 4a, PTFE) and with (Figure 4b, SiC) SPhP excitation. The three distances above the surface of 10 , 1 , and 0.1 μm represent the far-field, transitional, and electrostatic near-field regimes, respectively. In the far-field regime $\rho[10$ $\mu\text{m}, \omega]$ is dominated by states below the light line (white dashed) where

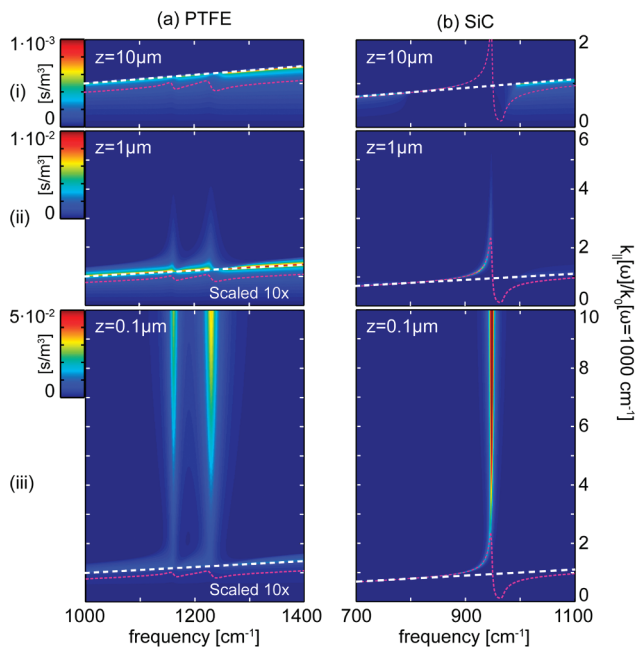


Figure 4. Calculated in-plane wavevector dependence of the local electromagnetic density of states (EM-LDOS) $\rho[z, \omega]$ above a surface for PTFE (a) and SiC (b) for the far-field (i), transitional (ii), and quasistatic near-field (iii) regimes represented by heights of 10, 1, and 0.1 μm respectively. The free-space light line dispersion (white dashed) marks the far (below) to near-field (above) transition while the material's surface wave dispersion relation (solid magenta) indicates the driving surface resonances.

$k_{||}$ corresponds to propagating modes. The near-field regime is characterized by $k_{||}$ above the light line representing evanescent fields. The magenta lines show the $k_{||}[\omega]$ which satisfy the SPhP dispersion relation.

PTFE represents a material with localized nondispersive molecular excitations. In the far-field (i) it exhibits characteristic broadband emission with only slight dips in $\rho[z, \omega]$ on resonance. As it fails to meet the surface polariton dispersion criterion, near-field enhancement occurs where $\text{Im}[\epsilon_{\text{PTFE}}]$ is maximal on resonance (ii, iii). As a consequence, and in agreement with experiment, the spectral near-field line-widths correspond to the far-field absorption line-widths also defined by $\text{Im}[\epsilon_{\text{PTFE}}]$.

In contrast, for SiC (Figure 4b) (with similar results for quartz, not shown), the enhancement of $\rho[z, \omega]$ is governed by the dispersion relationship for the SPhP. As a consequence, the peak magnitude of $\rho[z, \omega]$ is over 1 order of magnitude larger for SiC compared to PTFE. For SiC, as seen at a distance of 10 μm (i), the characteristic gap in the far-field propagating states ($k_{||} < k_0$) beginning at 1000 cm^{-1} is related to the high-reflectivity Reststrahlen band. In the transition regime at a distance of 1 μm (ii), an enhancement at energies below the SPhP resonance of 950 cm^{-1} following the surface wave dispersion relation develops. At short distances (iii) the distribution of EM-LDOS is governed by high wave-vector contributions located at the asymptote of the dispersion relation corresponding to the resonance condition for surface phonon-polariton excitation. This leads to the characteristic strong SPhP peak in the EM-LDOS responsible for the distinct spectral differences between the near-field and the far-field regime as observed in the experiment as well as the larger near-field response of SiC compared to PTFE.

To understand the detailed relationship between the tip-scattered thermal near-field signal and the underlying EM-LDOS, one has to consider that the detected near-field signal can be affected by the mutual optical polarization between the tip and the sample. Similar to conventional *s*-SNOM with external excitation illumination, here the radiating polarization in the tip is driven by the thermal evanescent field which in turn is affected by the resonant dielectric properties of the sample. Modeling the tip as a small off-resonant polarizable sphere, its effective polarizability as a function of distance above the surface z and radius r is given by

$$\alpha_{\text{eff}} = \alpha \left(1 - \frac{\alpha\beta}{16\pi(r+z)^3} \right)^{-1} \quad (2)$$

with $\beta = (\epsilon_2 - 1)/(\epsilon_2 + 1)$ relating the strength of the image dipole in the surface and $\alpha = 4\pi r^3[(\epsilon_{\text{sph}} - 1)/(\epsilon_{\text{sph}} + 2)]$ representing the Clausius–Mossotti relation for the polarizability of a sphere with dielectric permittivity ϵ_{sph} .^{20,21} The resulting optical polarization leads to a spectral distribution of the scattered power which can be expressed as the product of $u[z, \omega, T]$, the effective scattering cross-section of the sphere C_{eff} , and the speed of light c as

$$P_{\text{scat}}[z, \omega, T] = C_{\text{eff}} \cdot c \cdot u[z, \omega, T_{\text{surf}}] \quad (3)$$

Here, the effective scattering cross-section of the sphere C_{eff} is defined in terms of the effective polarizability as $C_{\text{eff}} = k^4 |\alpha_{\text{eff}}|^2 / (6\pi)$.³²

The resulting spectral distribution of the tip-scattered intensity induced by the near-field thermal spectral energy density for $T = 500$ K is plotted in Figure 2 (blue dashed line) for all three materials convolved with the ~ 25 cm^{-1} spectral resolution of our experiment. We find good general agreement between the experimentally observed results and the model for the scattered power by the tip given by eq 3. The scattered near-field power derived from the relationships above also agrees well with the 30–100 pW of near-field scattering power observed in our measurements.

The experimental results on SiC are reminiscent of laser *s*-SNOM spectroscopic measurements which exhibit a signal peak at 920 cm^{-1} .^{33,34} As in *s*-SNOM, eq 3 incorporates a optical phase related few cm^{-1} red shifts with line asymmetry due to the strong tip–sample coupling at short distances ($z \lesssim$ AFM tip apex radius).^{20,34} This effect is slightly more pronounced when considering details of tip geometry and higher-order mode coupling compared to the simple model above, but within the limits of the natural line width of molecular or phonon excitation. A 5–10 cm^{-1} red shift and spectral broadening is also expected from phonon softening and increased damping with temperature.^{35–38} We attribute these as the dominant effects, together with a higher defect density of the natural quartz measured, for the observed deviations from the model calculations. However, a detailed discrimination is not possible within the available spectral resolution and signal-to-noise ratio of our experiment.

For distances larger than the strong tip–sample coupling range of about the ~ 40 nm of the tip apex radius, TINS can thus serve as a measurement of the evanescent spectral energy distribution $u[z, \omega, T]$ and its resonances of the sample with the tip acting only as a weakly perturbing scatterer. The associated underlying near-field EM-LDOS, also for shorter distances, may be explicitly extracted using an appropriate

models that incorporates the dynamic variation of coupling with the tip-dither motion, the role of far-field interference and surface reflection, details of the tip geometry affecting coupling and scattering, as well as contributions due to variations in the surface topography.

Far-field thermal emission spectroscopy with its limited sensitivity has long been known as a useful technique for materials characterization especially where implementation of external light sources is not practical or even possible.^{39,40} Our work shows that the enhanced EM-LDOS in the thermal near-field associated with resonance modes enables infrared thermal near-field spectroscopy as a new scanning probe technique with IR vibrational contrast and spatial resolution determined by the EM-LDOS near-surface localization and/or tip apex radius.

The spatial resolution that we achieve is demonstrated in Figure 5 for a spectrally integrated TINS scan of a PTFE flake

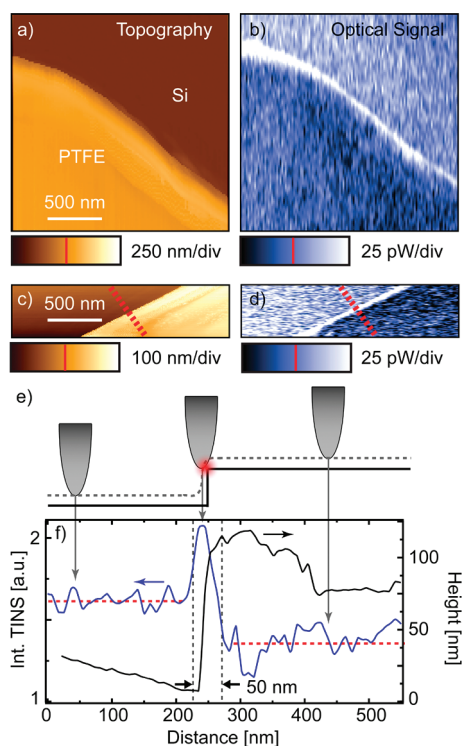


Figure 5. Topography (a,c) and spectrally integrated TINS signal (b,d) with contrast between a PTFE flake of thickness ~ 100 nm on a Si substrate. Panels c and d represent a higher resolution scan near the PTFE step edge with line-trace (f) of topography and TINS signal (laterally averaged over six scan lines, along red dashed line in c). An increase in scattering with the tip at the PTFE step edge is observed as indicated schematically in (e). The spatial resolution of ~ 50 nm as indicated by the vertical gray dashed lines (f) agrees with expectation related to tip apex radius.

boundary of thickness ~ 100 nm on a Si substrate. The line trace (f, laterally averaged over six lines in the high resolution scans c,d) indicates a spatial resolution of ~ 50 nm consistent with the tip apex radius. We interpret the enhanced signal at the PTFE step edge with elevated near-field coupling and scattering at the edge.

Using the spatial resolution data obtained from Figure 5, the sensitivity of the TINS measurement can be estimated for PTFE. Here, for a density of 2.2×10^6 g/m³ and a tip-apex localized sample volume of $\sim 1 \times 10^6$ nm³, the number of sampled C–F groups amounts to $\sim 5 \times 10^7$, corresponding to

~ 40 attomol of CF₂ groups. Modeling the statistical distribution of the PTFE CF₂ groups using the microcanonical partition function for a harmonic oscillator $Z^* = 1/(1 - \exp(-\hbar\omega/k_B T))$, an estimated 3–8% fraction of vibrationally excited oscillators contributes to the signal for temperatures in the 500–700 K range. Assuming a minimal signal-to-noise ratio of ~ 10 necessary for spectral peak assignment the resulting sensitivity for spectroscopic contrast is as high as 3–5 attomol.

This sensitivity represents an increase in IR-spectroscopic sensitivity of at least 4 orders of magnitude over conventional far-field IR microscopy techniques where spatial resolution is constrained by the diffraction limit (~ 10 μ m)⁴¹ and non-enhanced far-field absorption. The sensitivity is comparable to conventional laser-based s-SNOM,⁴² and can be further improved utilizing IR optical antenna modes of specially engineered tips. This implementation of s-SNOM with a heated tip thus allows for broadband chemical nanospectroscopy, complementary to the use of an external thermal light-source,⁴³ yet with higher sensitivity and the thermally driven vibrational optical dipoles providing their own intrinsic light source.

In summary, our spectroscopic characterization of the enhanced electromagnetic near-field spectral energy densities connect the previously well-defined regime of broadband far-field thermal radiation to the prediction of intrinsic and extrinsic thermal near-field resonances and their wave-vector distribution. The results open the door, for example, for tailoring heat management in microelectronic and thermophotovoltaic devices, optical antenna resonant control and switching of optical forces, enhanced IR and thermal sensing, and compact chemical nanoimaging and -spectroscopy instrumentation without the need for an external excitation source.

APPENDIX

Beyond the quasistatic near-field approximation, the full EM-LDOS for a planar system can be described as the sum of far-field radiative and evanescent contributions. For a semi-infinite planar half space the dielectric properties of the upper and lower half spaces are defined by complex frequency dependent permittivities $\epsilon_1[\omega]$ and $\epsilon_2[\omega]$, respectively. Combination of the Green's dyadic relating the field induced above the surface for a given current density element with the fluctuation–dissipation theorem describing the statistical nature of the current density fluctuations allows for the EM-LDOS to be expressed as an integral over the in-plane momentum k_{\parallel} phase-space.^{6,7}

$$\rho[z, \omega] = \frac{\rho_v[\omega]}{2} \left\{ \underbrace{\int_0^{\omega/c} \frac{k_{\parallel}}{k_0 |k_{1,\perp}|} \frac{2 - |r_{12}^s|^2 - |r_{12}^p|^2}{2} dk_{\parallel}}_{\text{propagating}} + \underbrace{\int_{\omega/c}^{\infty} \frac{4k_{\parallel}^3}{k_0^3 |k_{1,\perp}|} \frac{\text{Im}[r_{12}^s] + \text{Im}[r_{12}^p]}{2} e^{-2\text{Im}[k_{1,\perp}]z} dk_{\parallel}}_{\text{evanescent}} \right\} \quad (4)$$

with vacuum density of states $\rho_v = \omega^2/\pi^2 c^3$ and free-space wavevector k_0 . r_{12}^s and r_{12}^p represent the Fresnel reflection factors of the medium for s and p polarizations expressed as the in and out-of-plane components of the wavevector of the light, k_{\parallel} and $k_{n,\perp}$, as $r_{12}^s = (k_{1,\perp} - k_{2,\perp})/(k_{1,\perp} + k_{2,\perp})$ and $r_{12}^p = (\epsilon_2 k_{1,\perp}$

$-\varepsilon_1 k_{2,\perp})/(\varepsilon_2 k_{1,\perp} + \varepsilon_1 k_{2,\perp})$, respectively. Finally, k_{\parallel} and $k_{n,\perp}$ in the upper and lower half-space ($n = 1$ and $n = 2$) may be related to one another by the dispersion relation for light $\varepsilon_n \mu_n k_0^2 = k_{n,\perp}^2 + k_{\parallel}^2$ with $\text{Im}[k_{n,\perp}] > 0$ and $k_0 = \omega/c$.⁷ As seen in eq 4, in-plane wave-vectors k_{\parallel} smaller than the free-space wavevector k_0 correspond to propagating far-field solutions while those $k_{\parallel} > k_0$ correspond to nonpropagating evanescent fields.^{6,7}

In the far-field regime ($z \gg \lambda$), only in-plane wavevectors corresponding to propagating solutions in the first term of eq 4 contribute to the EM-LDOS ($k_{\parallel} < k_0$, $k_{1,\perp} \in \mathbb{R}e$). Here, the resulting far-field spectral energy density matches the classical solution defined by the emissivity ε and the Planck distribution $u_{\text{ff}}[\omega, T] = \varepsilon[\omega, T] \cdot \Theta[\omega, T]$.²⁶ While the far-field contribution to the EM-LDOS is still present for subwavelength distances from the surface $z < \lambda$, the contribution of the evanescent solution in eq 4 ($k_{\parallel} > k_0$ for which $k_{1,\perp} \in \mathbb{I}m$) now becomes a significant contribution to the total EM-LDOS.

In the quasi-static near-field limit ($z \ll \lambda$), the evanescent solutions are the dominant component of the EM-LDOS.^{6,7} These solutions are contained in the second integral term of eq 4. The contributions of a specific value of k_{\parallel} to the total EM-LDOS is negligible for $k_{\parallel} \gg (\lambda/4\pi z)$. This implies that in near-field regime large values of k_{\parallel} ($k_{\parallel} \gg k_0$) now make significant contributions to the total EM-LDOS. In this limit of large k_{\parallel} ($k_{\parallel} \rightarrow \infty$), the Fresnel reflection factors reduce to $r_{12}^s = 0$ and $r_{12}^p = (\varepsilon_2 - 1)/(\varepsilon_2 + 1)$. Here, the EM-LDOS may be approximated by the evanescent component described by the second integral term in eq 4, which further simplifies to

$$\rho_{\text{ev}}[z, \omega] \simeq \frac{1}{\pi^2 \omega |\varepsilon_2 + 1|^2} \int_{\omega/c}^{\infty} k_{\parallel}^2 \exp[-2k_{\parallel} z] dk_{\parallel} \quad (5)$$

The integration of eq 5 simplifies to the formula for the quasi-static scaling of the EM-LDOS given by eq 1. It is evident here, from the integral term in eq 5, that the contributions large wavevectors ($k \gg k_0$) are the primary component of the EM-LDOS.

With knowledge of the EM-LDOS calculated using eq 4, the spectral energy density above a specific surface material at a given temperature may be calculated by multiplying with the Planck distribution $u[z, \omega, T] = \rho[z, \omega] \Theta[\omega, T]$. Figure 6a displays the resulting $u[z, \omega, T]$ in the near-field regime above a SiC surface in the vicinity of the SPhP resonance frequency at 950 cm^{-1} . The associated scattering by the AFM-tip, modeled by the scattering of a small off-resonant polarizable sphere and calculated via eq 3 for a 20 nm Si sphere, is displayed in Figure 6b. Line-traces displaying the spectral distribution $u[z, \omega, T]$ and the associated spectral scattering power P_{scat} of the tip-sphere at heights of 10 and 40 nm above the surface are displayed in panels c and d of Figure 6 representing height to tip-radius ratios of 0.5 and 2, respectively.

At distances below the AFM tip-radius (panel c), the effect of mutual coupling between the tip and its image dipole leads to a slight ($\sim 5 \text{ cm}^{-1}$) redshift in the P_{scat} . Because of the narrow line-width of $u[z, \omega, T]$ associated with the SPhP resonance in the near-field limit, the magnitude of spectral shift in P_{scat} is constrained to the line-width of the peak in $u[z, \omega, T]$. Furthermore, the incorporation of surface reflection terms for the P_{scat} has only minimal effects on its spectral distribution. Finally, for heights greater than the tip-height (panel d), any effects due to mutual coupling with the surface are minimal, meaning that the scattering distribution of the nonresonant sphere directly reflects the intrinsic spectral distribution of $u[z, \omega, T]$.

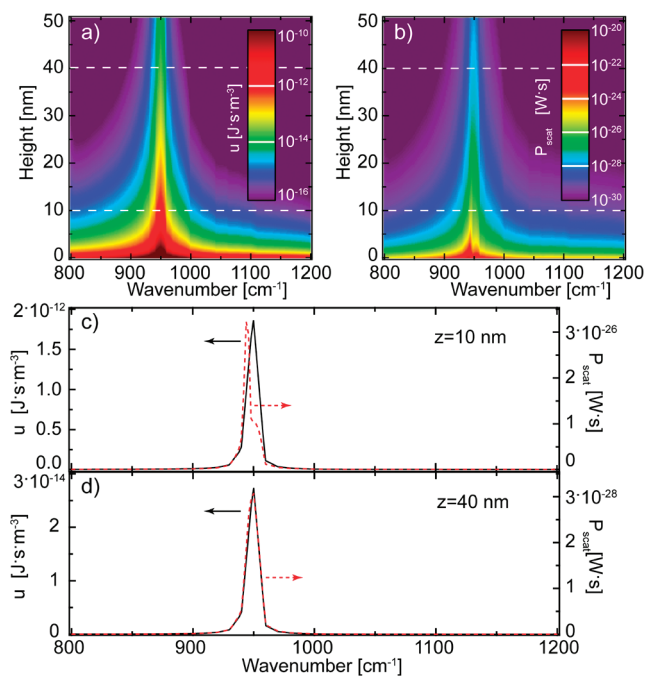


Figure 6. The height and spectral dependence of $u[z, \omega, 500 \text{ K}]$ (a) and $P_{\text{scat}}[z, \omega, 500 \text{ K}]$ (b) are displayed with logarithmic colorscales as calculated using eqs 4 and 3 for a Si sphere of radius $a = 20 \text{ nm}$. Panels (c) and (d) compare the spectral distributions of $u[z, \omega, 500 \text{ K}]$ and $P_{\text{scat}}[z, \omega, 500 \text{ K}]$ for heights of 10 and 40 nm, marked by the white dashed lines in panels (a) and (b), representing height-to-tip radius ratios of $z/a = 0.5$ and $z/a = 2$ respectively.

■ ASSOCIATED CONTENT

Supporting Information

Information on the TINS signal tip–sample distance dependence for a SiC surface is provided. This material is available free of charge via the Internet at <http://pubs.acs.org>.

■ AUTHOR INFORMATION

Corresponding Author

*E-mail: markus.raschke@colorado.edu.

Notes

The authors declare no competing financial interest.

■ ACKNOWLEDGMENTS

We gratefully acknowledge insightful discussions with Jean-Jacques Greffet and Eric Cornell and technical support from Kevin Kjoller (Anasys Instruments). The work has been supported by an DoE-STTR Grant (DE-FG02-08ER86338) and a NSF graduate fellowship.

■ REFERENCES

- (1) Kirchhoff, G. *Monatsber. preuss Akad.* **1859**, 783–87.
- (2) Planck, M. *Verh. Dtsch. Phys. Ges.* **1900**, 2, 237–245.
- (3) Hargreaves, C. M. *Phys. Lett. A* **1969**, 30, 491–492.
- (4) Polder, D.; Van Hove, M. *Phys. Rev. B* **1971**, 4, 3303–3314.
- (5) Shchegrov, A. V.; Joulain, K.; Carminati, R.; Greffet, J.-J. *Phys. Rev. Lett.* **2000**, 85, 1548–1551.
- (6) Joulain, K.; Carminati, R.; Mulet, J.-P.; Greffet, J.-J. *Phys. Rev. B* **2003**, 68, 245405.
- (7) Joulain, K.; Mulet, J.; Marquier, F.; Carminati, R.; Greffet, J. *Surf. Sci. Rep.* **2005**, 57, 59–112.
- (8) Fu, C.; Zhang, Z. *Int. J. Heat Mass Trans.* **2006**, 49, 1703–1718.

- (9) Shen, S.; Narayanaswamy, A.; Chen, G. *Nano Lett.* **2009**, *9*, 2909–2913.
- (10) Casimir, H. B. G.; Polder, D. *Phys. Rev.* **1948**, *73*, 360–372.
- (11) Lifshitz, E. *Dokl. Akad. Nauk SSSR* **1955**, *100*, 879.
- (12) Antezza, M.; Pitaevskii, L. P.; Stringari, S. *Phys. Rev. Lett.* **2005**, *95*, 113202.
- (13) Obrecht, J. M.; Wild, R. J.; Antezza, M.; Pitaevskii, L. P.; Stringari, S.; Cornell, E. A. *Phys. Rev. Lett.* **2007**, *98*, 063201.
- (14) Pendry, J. J. *Phys. Condens. Mat.* **1999**, *11*, 6621–6633.
- (15) Rousseau, E.; Siria, A.; Jourdan, G.; Volz, S.; Comin, F.; Chevrier, J.; Greffet, J.-J. *Nat. Photonics* **2009**, *3*, 514–517.
- (16) Kajihara, Y.; Kosaka, K.; Komiyama, S. *Rev. Sci. Instrum.* **2010**, *81*, 033706.
- (17) Wilde, Y. D.; Formanek, F.; Carminati, R.; Gralek, B.; Lemoine, P.; Joulain, K.; Mulet, J.; Chen, Y.; Greffet, J. *Nature* **2006**, *444*, 740–43.
- (18) Kittel, A.; Wischnath, U. F.; Welker, J.; Huth, O.; Ruting, F.; Biehs, S.-A. *Appl. Phys. Lett.* **2008**, *93*, 193109.
- (19) Rytov, S.; Kravtsov, Y.; Tatarskii, V. *Principles of Statistical Radiophysics*; Springer-Verlag: New York, 1978; Vol. 3, Chapter 3.
- (20) Raschke, M. B.; Lienau, C. *Appl. Phys. Lett.* **2003**, *83*, 5089–5091.
- (21) Hillenbrand, R.; Keilmann, F. *Philos. Trans. R. Soc. London, Ser. A* **2004**, *362*, 787–805.
- (22) Chapuis, P.-O.; Greffet, J.-J.; Joulain, K.; Volz, S. *Nanotechnology* **2006**, *17*, 2978–2981.
- (23) Behr, N.; Raschke, M. B. *J. Phys. Chem. C* **2008**, *112*, 3766–3773.
- (24) *Handbook of Optical Constants of Solids*; Palik, E., Ed.; Academic Press: New York, 1985; Vol. 1.
- (25) Korte, E. H.; Röseler, A. *Anal. Bioanal. Chem.* **2005**, *382*, 1987–1992.
- (26) McMahan, H. O. *J. Opt. Soc. Am.* **1950**, *40*, 376–378.
- (27) Liang, C. Y.; Krimm, S. *J. Chem. Phys.* **1956**, *25*, 563–571.
- (28) Moynihan, R. E. *J. Am. Chem. Soc.* **1959**, *81*, 1045–1050.
- (29) Spitzer, W. G.; Kleinman, D. A. *Phys. Rev.* **1961**, *121*, 1324–1335.
- (30) Scott, J. F.; Porto, S. P. S. *Phys. Rev.* **1967**, *161*, 903–910.
- (31) With the scattering power of the tip, $P_{\text{scat}}[z, \omega, T] \propto u[z, \omega, T]$, we here model the distance dependence of the TINS signal occurring at a frequency of ν_d as proportional to the quantity $\partial u / \partial z$ as the signal in dynamic *s*-SNOM measurements are primarily sensitive to the gradient of the optical near-field (see ref 44).
- (32) Bohren, C.; Huffman, D. *Absorption and Scattering of Light by Small Particles*; Wiley & Sons: New York, 1983.
- (33) Hillenbrand, R.; Taubner, T.; Keilmann, F. *Nature* **2002**, *418*, 159.
- (34) Cvitkovic, A.; Ocelic, N.; Hillenbrand, R. *Opt. Express* **2007**, *15*, 8550–8565.
- (35) Schuller, J. A.; Taubner, T.; Brongersma, M. L. *Nat. Photonics* **2009**, *3*, 658–661.
- (36) Otey, C. R.; Lau, W. T.; Fan, S. *Phys. Rev. Lett.* **2010**, *104*, 154301.
- (37) Gervais, F.; Piriou, B. *Phys. Rev. B* **1975**, *11*, 3944–3950.
- (38) Hafeli, A. K.; Rephaeli, E.; Fan, S.; Cahill, D. G.; Tiwald, T. E. *J. Appl. Phys.* **2011**, *110*, 043517–5.
- (39) Barr, J. *Infrared Phys.* **1969**, *9*, 97–108.
- (40) Chiang, S.; Tobin, R. G.; Richards, P. L.; Thiel, P. A. *Phys. Rev. Lett.* **1984**, *52*, 648–651.
- (41) Bechtel, H. A.; Martin, M. C.; May, T. E.; Lerch, P. *Rev. Sci. Instrum.* **2009**, *80*, 126106.
- (42) Raschke, M. B.; Molina, L.; Elsaesser, T.; Kim, D. H.; Knoll, W.; Hinrichs, K. *ChemPhysChem* **2005**, *6*, 2197–2203.
- (43) Huth, F.; Schnell, M.; Wittborn, J.; Ocelic, N.; Hillenbrand, R. *Nat. Mater.* **2011**, *10*, 352–356.
- (44) Olmon, R. L.; Rang, M.; Krenz, P. M.; Lail, B. A.; Saraf, L. V.; Boreman, G. D.; Raschke, M. B. *Phys. Rev. Lett.* **2010**, *105*, 167403.

■ NOTE ADDED AFTER ASAP PUBLICATION

This paper was published ASAP on February 8, 2012. The title of the paper has been updated. The revised version was posted on March 1, 2012.